Influence of boundary slip on the optimal excitations in thermocapillary driven spreading

Jeffrey M. Davis* and Sandra M. Troian†
Microfluidics Research & Engineering Laboratory, Department of Chemical Engineering, Princeton University, Princeton, New Jersey 08544-5263, USA
(Received 9 April 2003; revised manuscript received 2 July 2004; published 29 October 2004)

Thin liquid films driven to spread on homogeneous surfaces by thermocapillarity can undergo frontal breakup and parallel rivulet formation with well-defined wavelength. Previous modal analyses have relieved the well-known divergence in stress that occurs at a moving contact line by matching the front region to a precursor film. Because the linearized disturbance operator is non-normal, a generalized, nonmodal analysis is required to probe film stability at all times. The effect of the contact line model on nonmodal stability has not been previously investigated. This work examines the influence of boundary slip on thermocapillary driven spreading using a transient stability analysis, which recovers the conventional modal results in the long-time limit. In combination with earlier work on thermocapillary driven spreading, this study verifies that the dynamics and stability of this system are rather insensitive to the choice of contact line model and that the leading eigenvalue is physically determinant, thereby assuring results that agree with the eigenspectrum. Modal results for the flat precursor film model are reproduced with appropriate choice of slip coefficient and contact line slope.

DOI: 10.1103/PhysRevE.70.046309 PACS number(s): 47.15.Fe, 47.20.Dr, 47.54.+r, 47.62.+q

I. INTRODUCTION

Thin liquid films driven to spread over a smooth and chemically homogeneous surface provide an interesting system in which to study the evolution of instabilities at a moving front. Experiments have shown that both body forces, like centrifugation and gravity, and surface stresses, due to thermocapillary forces or a stream of gas directed along the film interface, can cause a flow transition from a uniform front to an array of parallel rivulets. A simple example of this instability can be seen in a paint film streaming down a vertical wall. During the past several years, there has been significant work in examining disturbance amplification in those systems using a generalized linear stability analysis suitable for non-normal systems. Some systems appear to undergo significant transient growth while others essentially reproduce the predictions of normal mode analysis. Because the instabilities occur in the vicinity of the moving contact line, more attention is being focused on the choice of boundary conditions used to relieve the usual stress singularity caused by the incompatibility of the no-slip condition with motion of the contact line. It would therefore be useful to understand precisely how the choice of contact line model affects the spatial and temporal evolution of the film profile and how this profile in turn influences the transient and asymptotic stability of driven films.

Previous studies of thermocapillary driven flow [1–4] utilized a precursor film to relieve the stress singularity at the moving contact line, which arises from the conventional no-slip boundary condition at the solid surface. Although both slip and precursor film models for coating flows driven by a body force have been examined via a modal stability analysis [5], the literature does not contain stability analyses of slip models for thermocapillary driven films. Expanding the work in the first part of this study [4], the present work incorporates a slip boundary condition at the solid surface and examines the effects of this model on the transient dynamics and amplification of optimal disturbances to the spreading film. The non-normality of the linearized disturbance operator is investigated through examination of the temporal evolution of the maximum disturbance amplification and plots of the pseudospectra. The results indicate that the transient amplification of disturbances is relatively unimportant for thermally driven films and that the stability predictions of different contact line models agree quantitatively.

II. GOVERNING EQUATIONS

A general equation governing the evolution of a thermally driven film within the lubrication approximation (including slip at the solid surface) has been derived previously [6], but the slip model was different, and no detailed examination of the velocity field was made. The derivation of the governing partial differential equation (PDE) is therefore given in some detail below. Consider the thermocapillary driven flow of a Newtonian liquid film of density ρ and viscosity μ. The liquid is supplied from a source at constant flux, and a constant thermal gradient is applied along the substrate such that the temperature decreases in the direction of spreading.

Assuming that the film is sufficiently thin that hydrostatic pressure and drainage are negligible, the lubrication equations that govern the motion of the liquid are

$$\mu\frac{\partial^2 u}{\partial z^2}=\frac{\partial p}{\partial x}=-\frac{\partial}{\partial x}(\gamma\nabla^2\tilde{h}),$$

*Present address: Department of Chemical Engineering, University of Massachusetts, Amherst, MA 01003, USA.
Electronic address: jmdavis@ecs.umass.edu
URL: http://www.ecs.umass.edu/che/faculty/davis.html
†Electronic address: stroian@princeton.edu
URL: www.princeton.edu/~stroian

$$\mu\frac{\partial^2 v}{\partial z^2}=\frac{\partial p}{\partial y}=-\frac{\partial}{\partial y}(\gamma\nabla^2\tilde{h}),$$

$$\mu\frac{\partial^2 w}{\partial z^2}=0, \tag{1}$$

where (u,v,w) are the components of the velocity in the streamwise, transverse, and normal directions relative to the substrate, (x,y,z) are the components of a Cartesian coordinate system in the respective directions, and $\tilde{h}$ is the film thickness. The boundary conditions are slip at the solid surface, based on the model proposed by Greenspan for spreading drops [7],

$$u|_{z=0}=u_s=\left.\frac{\tilde{\alpha}}{3\tilde{h}}\frac{\partial u}{\partial z}\right|_{z=0},$$

$$v|_{z=0}=v_s=\left.\frac{\tilde{\alpha}}{3\tilde{h}}\frac{\partial v}{\partial z}\right|_{z=0}, \tag{2}$$

and prescribed (constant) shear stress at the vapor-liquid interface,

$$\left.\mu\frac{\partial u}{\partial z}\right|_{z=\tilde{h}}=\frac{d\gamma}{dx}\equiv\tau,$$

$$\left.\mu\frac{\partial v}{\partial z}\right|_{z=\tilde{h}}=0. \tag{3}$$

The slip coefficient is represented by $\tilde{\alpha}$. Greenspan suggested that $\tilde{\alpha}\leqslant 10^{-14}$ m^2 but gave no rigorous justification for this choice. The resulting expressions for the streamwise and transverse components of the velocity are

$$u=\frac{-1}{\mu}\frac{\partial}{\partial x}(\gamma\nabla^2\tilde{h})\left(\frac{z^2}{2}-\tilde{h}z-\frac{\tilde{\alpha}}{3}\right)+\frac{\tau z}{\mu}+\frac{\tau\tilde{\alpha}}{3\mu\tilde{h}},$$

$$v=\frac{-1}{\mu}\frac{\partial}{\partial y}(\gamma\nabla^2\tilde{h})\left(\frac{z^2}{2}-\tilde{h}z-\frac{\tilde{\alpha}}{3}\right). \tag{4}$$

Although a singularity exists in the streamwise velocity at the contact line, the shear stress and flux ($\int_0^{\tilde{h}}u dz$) are well behaved. Furthermore, for sufficiently small values of the slip coefficient, the continuum model loses validity as $\tilde{h}\to 0$ well before the singularity becomes important. This singularity is not present in flow driven exclusively by a body force. An applied surface shear stress acts on an areal element of fluid and is incorporated into the velocity profile through a boundary condition. A body force acts on a volume element of the fluid, and the resulting additional power of $\tilde{h}$ in the shear stress at the solid surface negates the $\tilde{h}^{-1}$ in the slip model.

The kinematic condition at the material, vapor-liquid interface is expressed as

$$\frac{D\tilde{h}}{D\tilde{t}}=\left.w\right|_{z=\tilde{h}}, \tag{5}$$

where $D/D\tilde{t}$ denotes the material derivative. Integrating the incompressible form of the continuity equation with respect to z and substituting $w|_{z=\tilde{h}}$ from Eq. (5) yields the interface equation

$$\frac{\partial\tilde{h}}{\partial\tilde{t}}+\frac{\partial}{\partial x}\int_0^{\tilde{h}}u dz+\frac{\partial}{\partial y}\int_0^{\tilde{h}}v dz=0. \tag{6}$$

Substituting Eq. (4) into Eq. (6) yields a single partial differential equation that governs the evolution of the film thickness profile in the inner region near the contact line where effects of surface curvature are important:

$$\frac{\partial\tilde{h}}{\partial\tilde{t}}+\frac{\partial}{\partial x}\left[\frac{\tau\tilde{h}^2}{2\mu}\right]+\boldsymbol{\nabla}\cdot\left[\frac{1}{3\mu}(\tilde{h}^3+\mu\tilde{\alpha}\tilde{h})\boldsymbol{\nabla}(\gamma\nabla^2\tilde{h})\right]=0. \tag{7}$$

Equation (7) is converted to dimensionless form by introducing the transformations

$$\chi=-\frac{x}{l},\quad \zeta=\frac{y}{l},$$

$$h=\frac{\tilde{h}}{h_c},\quad t=\frac{\tilde{t}}{l/u_c}. \tag{8}$$

The dynamic capillary length $l=h_c/(3\mathrm{Ca})^{1/3}=(2\gamma_0 h_c^2/3\tau)^{1/3}$, with $\mathrm{Ca}=\mu u_c/\gamma$ the capillary number, is obtained by balancing the thermocapillary force against viscous and capillary forces. The characteristic Marangoni velocity of the thermally driven flow is given by $u_c\equiv h_c\tau/2\mu$, where h_c is the characteristic film thickness far from the leading edge where capillary effects are unimportant. The value γ_0 is evaluated at the same location as h_c

Assuming that the variation of surface tension with temperature makes a negligible contribution to the pressure gradient in the inner region of the flow, the dimensionless form of Eq. (7) is

$$h_t-(h^2)_\chi+\boldsymbol{\nabla}\cdot[(h^3+\alpha h)\boldsymbol{\nabla}\nabla^2 h]=0, \tag{9}$$

where $\boldsymbol{\nabla}\equiv\hat{\chi}\partial_\chi+\hat{\zeta}\partial_\zeta$ and subscripts denote partial differentiation with respect to χ, ζ, or t. The physical boundary conditions are vanishing film thickness at the contact line ($\chi=\chi_{CL}$), $h(\chi_{CL})=0$, prescribed contact slope $h_\chi(\chi_{CL})=\mathrm{C}_s$, and a flat film far from the contact line, $h\to 1$ and $h_{\chi\chi\chi}\to 0$ as $\chi\to\infty$.

III. BASE FLOW

A traveling-wave solution for the base flow that is constant in the moving frame $\xi=\chi+ct$ can be found by substituting $h(\chi,\zeta,t)=h_0(\xi)+\varepsilon h_1(\xi,\zeta,t)$ in Eq. (9), where $c=1$ is the wave speed and $\varepsilon\ll 1$. The position of the (unperturbed) contact line is given by $\xi=0$. Integrating the resulting ordinary differential equation (ODE) once and applying the boundary conditions yields

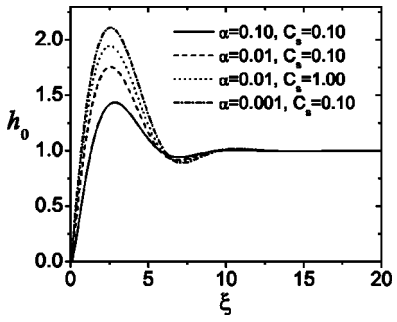

FIG. 1. Numerical solution of the dimensionless, steady-state profile $h_0(\xi)$.

$$h_{0\xi\xi\xi} = \frac{h_0 - 1}{h_0^2 + \alpha}, \tag{10}$$

subject to the conditions $h_0(0)=0$, $h_{0\xi}(0)=\mathsf{C}_s$, and $h_0 \to 1$ as $\xi \to \infty$. Equation (10) is solved numerically using a standard Runge-Kutta shooting method.

A. Steady-state solutions to base flow

Typical solutions for the height profile of the spreading film near the advancing front are shown in Fig. 1. Representative values of the slip coefficient are chosen to correspond to characteristic film thicknesses of a few microns, which are typical of many experimental investigations of thermally driven films. The contact slope is also varied from 0.10 to 1.00. Smaller values of C_s have only a small influence on the height profile and are not shown. The maximum amplitude of the capillary ridge increases with decreasing slip and increasing values of the slope at the contact line. For an appropriate choice of α and C_s that produces the same maximum amplitude of the capillary ridge as a precursor film of dimensionless thickness b, the base-state height profiles for the slip model and flat precursor film model are essentially indistinguishable. The base-state profile from the slip model with $\alpha=0.01$ and $\mathsf{C}_s=1.2035$ is compared to the profile from the precursor film model with $b=0.01$ in Fig. 2. The parameters were chosen so that the maximum amplitude of the capillary ridge is the same in either model and so that the contact line regions are similar, and the profiles cannot be distinguished on the scale of the plot. Such agreement is expected because the third order ODE's governing the base flows for the slip model and flat precursor film model [1] become identical as $\alpha \to 0$ and $b \to 0$. As shown in Fig. 2, strong agreement is attained even at finite values of α and b.

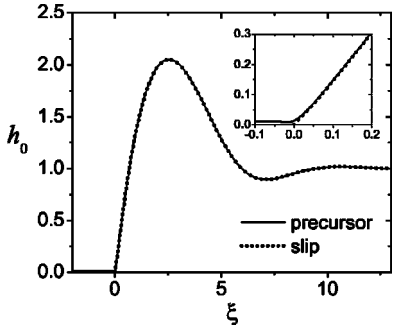

FIG. 2. Comparison of the base-state profiles from the slip model with $\alpha=0.01$ and $\mathsf{C}_s=1.2035$ and the precursor film model with $b=0.01$. The parameters were chosen such that the maximum amplitude of the capillary ridge is 2.051 89, and the two curves cannot be distinguished on the scale of the plot. The inset shows an enlarged view of the region near the contact line.

B. Stability analysis of steady-state solutions

In order to determine the stability of the spreading front to sinusoidal disturbances in the transverse direction, $\hat{\zeta}$, Eq. (9) is perturbed about the traveling-wave solution by the imposition of two-dimensional disturbances of the form

$$h_1(\xi,\zeta,t) = G(\xi,t)\exp(iq\zeta), \tag{11}$$

where the dimensionless wave number is defined as $q=k_w l$, with k_w the corresponding dimensional wave number and l the scaling appropriate for the inner region as defined in Eq. (8). The resulting (linearized) equation governing the evolution of the disturbance in the streamwise direction is

$$\frac{\partial G}{\partial t} = \left[2h_{0\xi} - \frac{(\alpha + 3h_0^2)(2h_0 + \alpha - h_0^2)h_{0\xi}}{(h_0^2+\alpha)^2} - \alpha q^4 h_0 - q^4 h_0^3 - \frac{6h_0 h_{0\xi}(h_0-1)}{h_0^2+\alpha} \right] G + \left[-1 + 2h_0 + 3q^2 h_0^2 h_{0\xi} + \alpha q^2 h_{0\xi} - \frac{(\alpha + 3h_0^2)(h_0-1)}{h_0^2+\alpha} \right] G_\xi + (2\alpha q^2 h_0 + 2q^2 h_0^3) G_{\xi\xi} + (-\alpha h_{0\xi} - 3h_0^2 h_{0\xi}) G_{\xi\xi\xi} + (-\alpha h_0 - h_0^3) G_{\xi\xi\xi\xi}. \tag{12}$$

This equation is subject to the decay conditions G, $G_\xi \to 0$ as $\xi \to \infty$ since the perturbation should not affect the outer region of the flow. At $\xi=0$, the boundary conditions are

$$h_{0\xi\xi} G - \mathsf{C}_s G_\xi = 0, \tag{13}$$

which is derived from a Taylor series expansion of h and h_ξ about $\xi=\xi_{CL}$ [5], and

$$G_t - (\mathsf{C}_s + \alpha q^2 h_{0\xi\xi}) G + \alpha \mathsf{C}_s G_{\xi\xi\xi} = 0, \tag{14}$$

which ensures that continuity is satisfied at the contact line. This last boundary condition can be derived by linearizing a kinematic condition describing the motion of the contact line or by evaluating Eq. (12) at $\xi=0$ and using Eq. (13). Discretizing Eq. (12) in space using a central difference scheme

yields a system of equations that can be expressed in operator form as

$$\frac{\partial \boldsymbol{G}}{\partial t} = \mathbf{A}\boldsymbol{G}. \tag{15}$$

The linear autonomous matrix $\mathbf{A}(\xi)$ that acts on the state of the system $\boldsymbol{G}(t)$ contains the elements obtained from the discretization and is real, nondefective, and non-normal.

IV. INVESTIGATION OF NON-NORMALITY

A. Linear stability theory

The traditional approach to hydrodynamic stability proceeds through modal analysis, which assumes exponential time dependence and reduces the analysis of Eq. (15) to solving the eigenvalue problem $\Delta_{ii}\boldsymbol{G}=\mathbf{A}\boldsymbol{G}$ for the eigenvalues Δ_{ii} of $\mathbf{A}$. Although accurate for flows governed by *normal* operators [8], this traditional analysis can break down if $\mathbf{A}$ is *non-normal*, in that $\mathbf{A}$ does not commute with its adjoint or, equivalently, does not have an orthogonal set of eigenvectors. The adjoint $\mathbf{A}^\dagger$ of $\mathbf{A}$ is defined by $(\boldsymbol{u},\mathbf{A}\boldsymbol{v})=(\mathbf{A}^\dagger\boldsymbol{u},\boldsymbol{v})$ for all $\boldsymbol{u}$, $\boldsymbol{v}$ in the domain of $\mathbf{A}$, where $(\cdot,\cdot)$ denotes the inner product.

The results of modal analysis are always valid if $\mathbf{A}$ is a compact normal operator [9]. For a non-normal operator, however, traditional modal theory only predicts the asymptotic behavior of solutions to the linearized equation as $t\to\infty$ and may prove inaccurate on the time scales of physical relevance. Investigations of the linear stability of disturbances governed by non-normal operators must therefore proceed beyond simple modal analysis to ensure the physical relevance of the results [10–13].

B. Optimal perturbation growth

The solution to Eq. (15) is the operator exponential acting on the initial condition $\boldsymbol{G}_0$:

$$\boldsymbol{G}(t) = \exp(t\mathbf{A})\boldsymbol{G}_0. \tag{16}$$

The maximum amplification $\sigma_{\max}$ of any initial perturbation over time t is [13]

$$\sigma_{\max}(t) \equiv \sup_{G_0\neq 0}\frac{\|G\|}{\|G_0\|} = \|\exp(t\mathbf{A})\|, \tag{17}$$

where the Euclidean norm is used. A nondefective matrix $\mathbf{A}$ has the similarity transform

$$\mathbf{A} = \mathbf{S}\boldsymbol{\Delta}\mathbf{S}^{-1}, \tag{18}$$

where $\mathbf{S}$ is the matrix whose columns are the normalized eigenvectors of $\mathbf{A}$ in order of growth rate and $\boldsymbol{\Delta}$ is the diagonal matrix of the associated eigenvalues [14]. It follows that

$$\exp(\Delta_{11}t) \leqslant \|\exp(t\mathbf{A})\| = \|\mathbf{S}\exp(t\boldsymbol{\Delta})\mathbf{S}^{-1}\| \leqslant \|\mathbf{S}\|\|\mathbf{S}^{-1}\|\exp(\Delta_{11}t), \tag{19}$$

where Δ_{11} is the leading entry of $\boldsymbol{\Delta}$. If $\mathbf{A}$ is normal, $\mathbf{S}$ is unitary, and $\|\exp(t\mathbf{A})\|=\exp(\Delta_{11}t)\,\forall\, t$. If $\mathbf{A}$ is non-normal, however, the eigenvectors are not orthogonal, and the norm of $\mathbf{S}$ and its inverse can be much greater than unity. Several orders of magnitude of transient amplification could occur and induce nonlinear effects, thereby invalidating the results of modal analysis [13].

Since $\exp(\mathbf{A}t)=\mathbf{S}\exp(t\boldsymbol{\Delta})\mathbf{S}^{-1}$, in the limit $t\to\infty$ the first column of $\mathbf{S}$ and the first row of $\mathbf{S}^{-1}$ exponentially dominate with amplification factor $\exp[\mathrm{Re}(\Delta_{11}t)]$. Applying Schwartz's inequality reveals that the normalized initial condition that produces the maximum growth over time t is the leading eigenvector of $\mathbf{A}^\dagger$, which is the leading adjoint eigenvector of $\mathbf{A}$. Formally, the spectral abscissa of $\mathbf{A}$, $\alpha(\mathbf{A})$, is equal to the growth abscissa $\gamma(\mathbf{A})$ [15]:

$$\alpha(\mathbf{A}) \equiv \sup_{z\in\Lambda(\mathbf{A})}\mathrm{Re}(z) \equiv \mathrm{Re}[\lambda_{\max}(\mathbf{A})] = \gamma(\mathbf{A}) \equiv \lim_{t\to\infty} t^{-1}\ln\|e^{t\mathbf{A}}\|, \tag{20}$$

which demonstrates that the results from modal analysis are recovered as $t\to\infty$.

C. Optimal perturbations

To determine the evolution of an optimal initial state into its final state at time t, the singular value decomposition of $\exp(t\mathbf{A})$ is calculated according to [13]

$$\exp(t\mathbf{A}) = \mathbf{U}\boldsymbol{\Sigma}\mathbf{V}^\dagger, \tag{21}$$

where the columns of the unitary matrix $\mathbf{V}$ represent the complete set of initial states and the columns of the unitary matrix $\mathbf{U}$ are orthonormal basis vectors that span the range space of final states. The diagonal matrix $\boldsymbol{\Sigma}$ contains elements σ_i that describe the growth of each corresponding initial state during the specified time interval. Note that the singular value decomposition must be calculated for each time at which $\mathbf{U}$, $\boldsymbol{\Sigma}$, and $\mathbf{V}$ are sought. For an initial perturbation $\boldsymbol{G}_0=\Sigma a_i\boldsymbol{V}_i$ with $\Sigma|a_i|^2=1$, applied at time $t=0$, the corresponding evolved state at time t is $\boldsymbol{G}=\Sigma a_i\sigma_i\boldsymbol{U}_i=\exp(t\mathbf{A})\boldsymbol{G}_0$. The vectors $\boldsymbol{V}_i$, which form the columns of $\mathbf{V}$, are ordered by growth; the optimal perturbation at a specified time, $\boldsymbol{V}_{\mathrm{opt}}\equiv\boldsymbol{V}_1$, is defined as the initial condition that generates the maximum growth over the time interval t. This maximum growth is defined by the leading singular value $\sigma_{\max}\equiv\|\exp(t\mathbf{A})\|$. Since all experimental studies of thermocapillary fingering phenomena have demonstrated the predominance of a single unstable wavelength, the initial states examined in this study are characterized by monochromatic disturbances $\mathbf{V}(\xi,q)$.

The maximum possible amplification at any time is attained by the optimal initial disturbance calculated for that time. As $t\to\infty$, the evolved state $\sigma_{\max}\boldsymbol{U}_{\mathrm{opt}}$, corresponding to the optimal initial condition with a wave number that induces the largest growth over all time, evolves into the eigenfunction that describes fingered growth in the spanwise direction, $\boldsymbol{H}(\xi)$. The optimal initial disturbance $\boldsymbol{V}_{\mathrm{opt}}(t\to\infty)$ in this long-time limit (at which the most unstable mode dominates) asymptotes to $\boldsymbol{H}^\dagger(\xi)$, the eigenvector of the adjoint linearized operator, which is the initial condition that optimally excites the most unstable mode. (Slight differences may occur at the ends of the domain due to the imposition of the physical

boundary conditions on the adjoint eigenvector.) For normal **A**, the optimal initial condition for any time is simply the normalized leading eigenvector.

D. ϵ-pseudospectrum

Determining the magnitude of the resolvent, $(z\mathbf{I}-\mathbf{A})^{-1}$, where **I** is the identity matrix, for a range of $z \in \mathbb{C}$ provides useful information regarding the behavior of the matrix **A** (and the operator of which it is the discrete representation) that cannot be determined by merely computing the eigenvalues. For each $\epsilon \geqslant 0$, the ϵ-pseudospectrum of **A** is defined as [15]

$$\Lambda_\epsilon(\mathbf{A}) = \{z \in \mathbb{C}: \|(z\mathbf{I}-\mathbf{A})^{-1}\| \geqslant \epsilon^{-1}\}. \tag{22}$$

If **A** is normal, then $\Lambda_\epsilon(\mathbf{A})$ (in the two-norm) is the union of discs formed by the set of points in $\mathbb{C}$ within a distance ϵ of the spectrum of **A**, $\Lambda(\mathbf{A})$. The ϵ-pseudospectrum may be much larger if **A** is non-normal. Examination of plots of $\Lambda_\epsilon(\mathbf{A})$ gives an indication of the extent of non-normality in a matrix and thus of the physical relevance of its eigenvalues. In any norm, difficulty arises if the basis of eigenvectors is ill conditioned. If an arbitrary vector is expressed terms of the eigenvector basis, the expansion coefficients may be extremely large relative to the magnitude of the vector itself. The relevant physics of the system may then be dominated by the evolving pattern of cancellation of these coefficients rather than by the behavior of individual eigenvalues. Stability predictions based on the eigenvalues could therefore be unreliable. An equivalent definition of the pseudospectra is [15]

$$\Lambda_\epsilon(\mathbf{A}) = \{z \in \mathbb{C}: z \in \Lambda(\mathbf{A}+\mathbf{E}) \text{ for some } \mathbf{E} \text{ with} \|\mathbf{E}\| \leqslant \epsilon\}. \tag{23}$$

This definition of the ϵ-pseudospectrum in terms of eigenvalues of perturbed matrices reveals that the pseudospectra can be used to assess the susceptibility of eigenvalues to perturbations (and thus give an indication of the accuracy of the eigenvalues).

If contours for $\epsilon \ll 1$ are visible on an $O(1)$ scale, then **A** is highly non-normal. The eigenvalues in that region of the complex *z* plane are nearly linearly dependent and can interact. These eigenvalues are also highly susceptible to perturbations, as indicated by Eq. (23). They may also be difficult to compute accurately and are of dubious physical relevance. If such contours for $\epsilon \ll 1$ are visible around the leading (least stable) eigenvalue, then stability predictions based on the eigenvalues may be inaccurate. Further analysis and computation of $\|\exp(t\mathbf{A})\|$ is warranted. If contours for small ϵ are not visible and **A** appears close to normal, then the eigenvalues should be accurate and sufficient to assess the stability of the physical system.

The pseudospectra of an operator or matrix also can be used to calculate bounds on $\|\exp(t\mathbf{A})\|$. A lower bound on the norm of the matrix exponential, derived from the Laplace transform and stated as part of the Kreiss matrix theorem, is given for any $\epsilon > 0$ by [15]

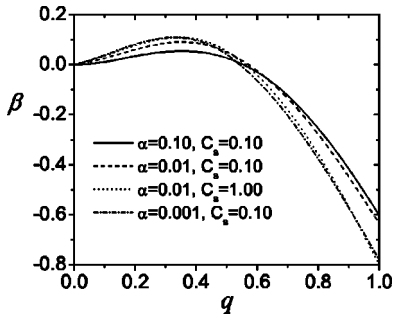

FIG. 3. Dispersion curves $\beta(q)$ from eigenvalue analysis corresponding to the base-state profiles shown in Fig. 1.

$$\sup_{t \geqslant 0} \|\exp(t\mathbf{A})\| \geqslant \epsilon^{-1} \sup_{z \in \Lambda_\epsilon(\mathbf{A})} \mathrm{Re}(z). \tag{24}$$

This bound is relevant if the spectrum is confined to the left half-plane since a lower bound on the transient growth can quickly be found by determining how far the pseudospectra extend into the right half-plane. If the spectrum extends into the right half-plane, then this bound is not useful since the growth becomes infinite as $t \to \infty$. Other bounds can also be constructed [15,16].

V. LINEAR STABILITY RESULTS

A. Eigenvalue analysis

The behavior of solutions of Eq. (12) at long times is determined by seeking an exponential solution of the form

$$G(\xi,t) = H(\xi)\exp(\beta t), \tag{25}$$

where β denotes the disturbance growth rate. The value of β with largest real part is the leading eigenvalue of **A**, Δ_{11}. Equation (15) becomes $\beta \boldsymbol{H} = \mathbf{A}\boldsymbol{H}$, and the eigenvalues and eigenfunctions of $\mathbf{A}(\xi)$ are calculated using the *eig* function in MATLAB 5.3. The dispersion curves $\beta(q)$, corresponding to the four base state height profiles shown in Fig. 1, are plotted in Fig. 3. There is a band of unstable wave numbers $0 < q \lesssim 0.55$ with the maximum growth rate occurring at $q_{\max} \approx 0.35$. The growth rate of the most unstable wave number increases as the slip coefficient α decreases or the contact slope C_s increases, both of which correspond to an increase in the amplitude of the capillary ridge. The largest eigenvalue for the base flow with $\alpha = 0.01$ and $C_s = 1.00$ is nearly as large as for the base flow with $\alpha = 0.001$ and $C_s = 0.10$.

The dispersion curves for the slip model with $\alpha = 0.10$, $C_s = 0.10$; $\alpha = 0.01$, $C_s = 1.00$; and $\alpha = 0.01$, $C_s = 1.2035$ are plotted with the dispersion curves for the flat precursor film model with $b = 0.10$ and $b = 0.01$ in Fig. 4. For an appropriate choice of parameters, the unstable portions of the dispersion curves overlap almost completely. Although the base state profiles for $\alpha = 0.01$, $C_s = 1.2035$, and $b = 0.01$ are nearly identical, as shown in Fig. 2, the slip model yields slightly larger eigenvalues for the unstable wave numbers $0 < q \lesssim 0.55$, so the dispersion curves do not overlap. While the base state for $\alpha = 0.01$, $C_s = 1.00$ has a slightly lower capillary ridge, the dispersion curves for these parameter values almost entirely overlap those for $b = 0.01$ for the range of q shown in Fig. 4.

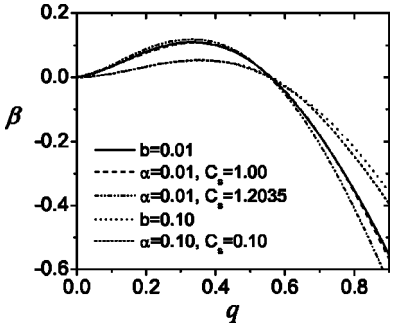

FIG. 4. Comparison of dispersion curves from the flat precursor film model with those from the slip model. The portions of the curves corresponding to unstable wave numbers overlap almost completely for an appropriate choice of parameters, although there is some deviation for large q.

B. Nonmodal analysis

The behavior of solutions to Eq. (12) at any time is determined by examining the time dependence of $\|\exp(t\mathbf{A})\|$ in the Euclidean norm. The evolution of an initial disturbance to its state after an arbitrary time t is also investigated. An emphasis of this investigation is the reason for which the traditional modal description of linear stability yields such accurate predictions for the non-normal disturbance operator that governs thermally driven, thin-film flows.

1. Amplification ratio

MATLAB 5.3 was used to calculate matrix norms and singular value decompositions. The number of grid points used to determine the discretized elements comprising matrix **A** ranges from 1000 to 4500 points. Experimental results published in the literature [17–19] demonstrate rivulet formation for dimensionless times in the range $t \lesssim 15$. The transient growth calculations are extended through a dimensionless time $t=40$, so the transient dynamics leading to rivulet formation should be adequately captured.

Figure 5 depicts the temporal evolution of $\ln\|\exp(t\mathbf{A})\|$ for selected dimensionless wave numbers q. This curve is the envelope (maximized over all initial conditions) of the amplification of individual initial conditions. Each point on the curve represents the maximum amplification of a different initial condition (the optimal for that time). There initially is a very small spike of transient amplification (less than e^1) for each wave number as the contact line adjusts to the imposed disturbance. Exponential growth at the rate predicted from the modal theory is approached by time $t \approx 5-10$ for almost every wave number, and the rapid attainment of this "long-time" limit explains the agreement between the experimentally observed initial finger growth rate and the eigenvalue predicted from modal analysis [1].

This convergence to the modal growth rate demonstrates complete agreement between the transient analysis at long times and the results of eigenvalue analysis, which must occur since, as indicated by Eq. (20), the asymptotic stability of the system as $t \to \infty$ is governed by $\exp(\Delta_{11} t)$, and the eigenvalue Δ_{11} is the β found from the modal theory. This mathematically required agreement therefore serves as a check on the numerical schemes used.

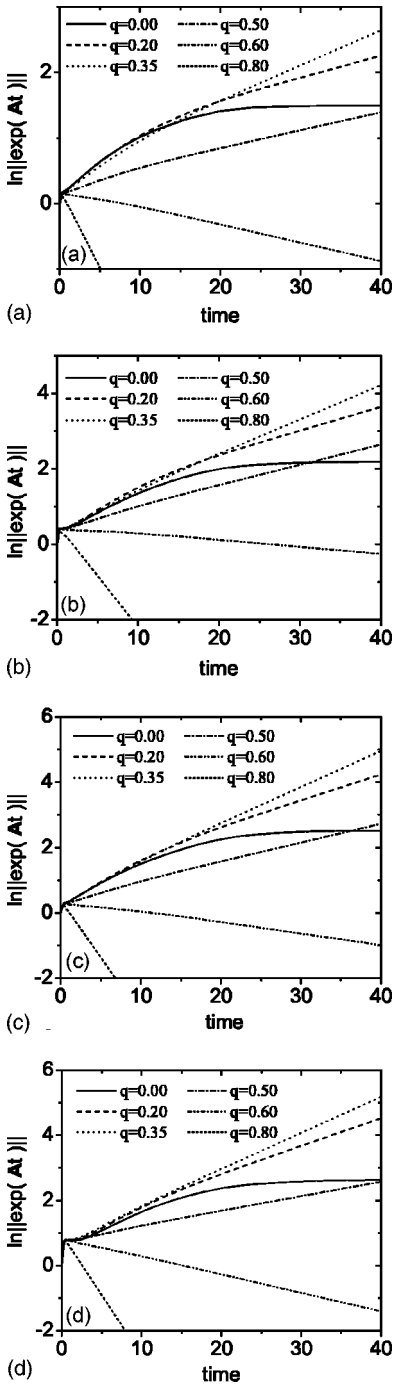

FIG. 5. Maximum possible amplification of disturbances within a time interval t for the height profiles shown in Fig. 1(a). The parameter values are (a) $\alpha=0.10$, $C_s=0.10$, (b) $\alpha=0.01$, $C_s=0.10$, (c) $\alpha=0.01$, $C_s=1.00$, and (d) $\alpha=0.001$, $C_s=0.10$.

2. Optimal perturbations

Plotted in Figs. 6–8 are the optimal initial states $\boldsymbol{V}_{\text{opt}}$ and the final states $\boldsymbol{G}=\sigma_{\max}\boldsymbol{U}_{\text{opt}}$, corresponding to the system's response after time t to monochromatic disturbances of representative transverse wave numbers q for $\alpha=0.10$ and C_s

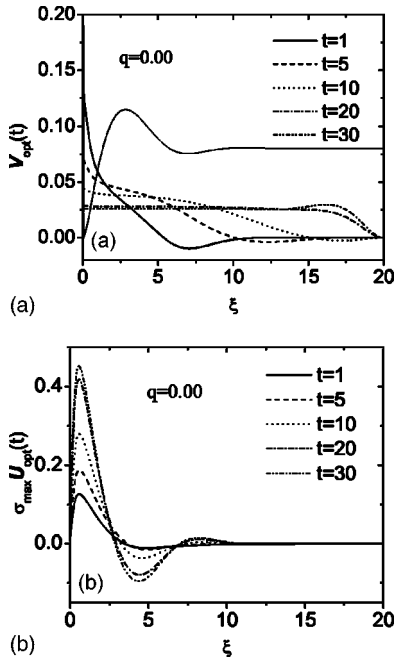

FIG. 6. (a) Optimal initial disturbance $\boldsymbol{V}_{\mathrm{opt}}$ and (b) the evolved state $\sigma_{\max}\boldsymbol{U}_{\mathrm{opt}}$ after time t for a disturbance of wave number $q=0.00$ applied to the base state with $\alpha=0.10$ and $\mathsf{C}_s=0.10$. Each initial disturbance is normalized to unit magnitude, and the magnitude of the corresponding evolved state is equal to the amplification attained by the initial disturbance at time t. The renormalized base state is superimposed in (a) to indicate which areas of the spreading film are most vulnerable to perturbations.

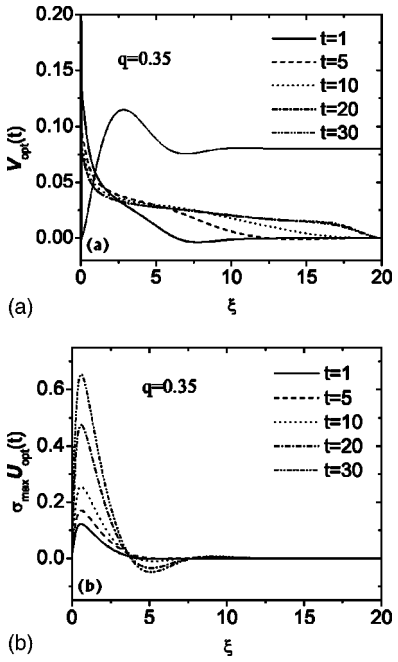

FIG. 7. (a) Optimal initial disturbance $\boldsymbol{V}_{\mathrm{opt}}$ and (b) the evolved state $\sigma_{\max}\boldsymbol{U}_{\mathrm{opt}}$ after time t for a disturbance of wave number $q=0.35$ applied to the base state with $\alpha=0.10$ and $\mathsf{C}_s=0.10$. Each initial disturbance is normalized to unit magnitude, and the magnitude of the corresponding evolved state is equal to the amplification attained by the initial disturbance at time t. The renormalized base state is superimposed in (a) to indicate which areas of the spreading film are most vulnerable to perturbations.

$=0.10$. The optimal initial and final states for other values of the slip coefficient and contact slope are very similar to those shown in Figs. 6–8. The initial states are normalized to have unit magnitude, and the magnitude of the evolved states corresponds to the amplification that an initial condition of unit magnitude attains at time t.

The optimal initial excitations and evolved states for the neutrally stable wave number $q=0$ are plotted in Fig. 6. The optimal initial disturbances are similar to those for unstable wave numbers, as is expected since disturbances with wave number $q=0$ experience growth at short times before asymptotically approaching a constant magnitude as $t\to\infty$. These optimal disturbances for short times are centered at the contact line but broaden to excite the entire spreading film nearly uniformly for longer times. The slight bump near $\xi=17$ in the disturbances calculated for later times results from the imposition of the physical boundary conditions, which force the excitation to zero at the end of the domain ($\xi=20$), which is taken to represent $\xi\to\infty$ numerically. [The adjoint eigenvector for $q=0$ is a constant, as is found by integrating Eq. (12) by parts to derive the adjoint operators, inspection of which reveals that $\boldsymbol{H}^{\dagger}=$const. is the null adjoint eigenfunction [20]. This result is also confirmed numerically.] This bump moves to remain several units away from the end of the domain when the domain is successively extended to $\xi=75$ but has no further effect on the results. It is straightforward to show analytically that the zero eigenvalue mode for $q=0$ is a constant multiple of the first derivative of the height profile for the base state, $h_{0\xi}$. The evolved state at time $t=30$, the corresponding modal eigenfunction, and $h_{0\xi}$ are indistinguishable (not shown).

The excitations for the most asymptotically unstable wave number $q=0.35$ are plotted in Fig. 7. The disturbance applied at $t=0$ that elicits the largest response at $t=1$ is localized at the contact line. The initial disturbances that elicit the maximal system response at later times broaden to encompass much of the capillary ridge but retain maxima at the contact line. The system's response to these perturbations initially is narrowly focused at the contact line and forward portion of thecapillary ridge but broadens at later times to encompass more of the capillary ridge. By a dimensionless time $t=15$ this response to the optimal disturbance is nearly indistinguishable from the eigenfunction determined from the standard modal theory.

Figure 8 contains plots of the optimal initial excitations and evolved responses for an asymptotically stable wave number $q=0.60$ for dimensionless times ranging from $t=1$ to $t=40$. The optimal initial excitations at early times are localized at the contact line, as they are for unstable wave numbers. The excitations that induce the optimal response at later times, however, do not broaden to encompass any of the capillary ridge. The system's response to the optimal disturbance for $t=1$ displays an oscillation minimum in the region corresponding to the capillary ridge, but this minimum is not nearly as pronounced as it is for unstable wave numbers and is not present in the evolved disturbances for later times. Comparatively more of the weight of the system's response is focused near the contact line than for unstable wave num-

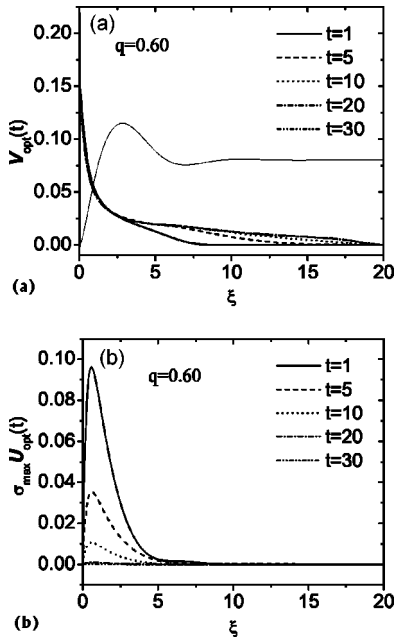

FIG. 8. (a) Optimal initial disturbance $\boldsymbol{V}_{\mathrm{opt}}$ and (b) the evolved state $\sigma_{\max}\boldsymbol{U}_{\mathrm{opt}}$ after time t for a disturbance of wave number $q=0.60$ applied to the base state with $\alpha=0.10$ and $\mathsf{C}_s=0.10$. Each initial disturbance is normalized to unit magnitude, and the magnitude of the corresponding evolved state is equal to the amplification attained by the initial disturbance at time t. The renormalized base state is superimposed in (a) to indicate which areas of the spreading film are most vulnerable to perturbations.

bers. Corresponding plots for other asymptotically stable wave numbers are similar to those shown for $q=0.60$. The differences between Figs. 7 and 8 indicate that while the initial perturbations that induce the optimal system response at later times for unstable wave numbers encompass the capillary ridge, the analogous excitations for stable wave numbers do not.

3. Investigation of the ϵ-pseudospectrum

Close approximations to the ϵ-pseudospectrum were calculated using the pseudospectra GUI [21] for MATLAB. Results for wave numbers $q=0.00$, 0.35, and 0.60 are shown in Fig. 9 with the physical decay boundary conditions imposed at the end of the numerical domain at $\xi=75$. The first column contains the pseudospectra for $\alpha=0.10$ and $\mathsf{C}_s=0.10$, and the second column contains those for $\alpha=0.01$ and $\mathsf{C}_s=1.00$. Contours are shown for $\epsilon=10^{-1},10^{-2},\ldots,10^{-11}$. The abscissa is $\mathrm{Re}(z)$, and the ordinate is $\mathrm{Im}(z)$. Near the leading eigenvalue, each ϵ-pseudospectral contour exceeds the spectrum by a distance only slightly greater than ϵ, and the eigenvalue with largest real part therefore appears physically determinant.

Each of the plots exhibits the most non-normality around the complex eigenvalues near $\mathrm{Re}(z)\approx-0.2$ because the $\epsilon=10^{-11}$ contours are visible in this region on an $O(1)$ scale. If the operator were normal, these contours would only extend 10^{-11} units beyond the eigenvalues and would not be visible in the figure. As the angles between the subspaces defined by given eigenvectors decrease, indicating that these eigenvectors are far from orthogonal, the ϵ-pseudospectral contours near the corresponding eigenvalues extend further from the spectrum. Eigenvalues in the regions of the plot in which the contours with the smallest ϵ are visible are therefore the most susceptible to perturbations, and the corresponding eigenvectors are closely aligned.

Explicit computation reveals that the angles between the subspaces defined by the eigenvectors associated with the complex conjugate eigenvalues are as low as about 3.5°. For any value of q, these eigenvectors are not nearly as closely aligned with the leading eigenvector. The nonmodal growth is primarily due to the interaction of specific stable eigenvectors with the leading eigenvector, which is evident in Fig. 9 and is quantified by the spectral projection of the optimal perturbations [22]. The projection of the optimal perturbations determined in Sec. V B 2 on the eigenvectors reveals the extent to which each eigenvector contributes to the optimal perturbations. Computation of these spectral projections (which are the coefficients of the optimal perturbation in the eigenvector basis) demonstrates that the complex conjugate eigenvalues do not significantly contribute to the optimal initial disturbances because the projections on the associated eigenvectors are small. This weak contribution explains the insensitivity of $\|\exp(t\mathbf{A})\|$ to the length of the computational domain even though the domain length has a strong effect on the determination of these complex eigenvalues, as noted below. Because of the large spectral projection of the optimal disturbances on the leading eigenvector (indicating that, even at early times, the optimal disturbances resemble the leading adjoint eigenvector), little transient growth occurs. For each wave number, although the values of α and C_s change by an order of magnitude from one set of plots to the other, the degree of non-normality increases only slightly, as evident in the similarities between the plots. This apparently small increase is consistent with the small increase in transient growth displayed in the plots of $\ln\|\exp(t\mathbf{A})\|$ vs t shown in Fig. 5.

In addition, the spectrum (and hence the pseudospectra) of the operator depends on the length of the domain used, especially for small q. This dependence is caused by the physical decay boundary conditions as $\xi\rightarrow\infty$—i.e., the end of the finite numerical domain corresponding to the inner region of the flow. Increasing the end of the domain from $\xi=25$ to $\xi=75$ increases the number of pairs of complex conjugate eigenvalues near $\mathrm{Re}(z)\approx-0.2$ from 2 to 8 for $q=0$. Longer domains do not change the spectra significantly. The pseudospectra indicate that these eigenvalues are the most susceptible to perturbation and therefore the most difficult to determine accurately. Because the extent of non-normality in this region of the complex z plane is high, these eigenvalues may not be physically significant, but accurate computation of these subdominant eigenvalues is not important for stability predictions.

Although the structure of the pseudospectra therefore changes in the region of the complex plane near $\mathrm{Re}(z)\approx-0.2$, the region around the most unstable eigenvalue is essentially unaffected. These results indicate that the leading eigenvalue remains physically determinant and that the amount of transient amplification is similar for computa-

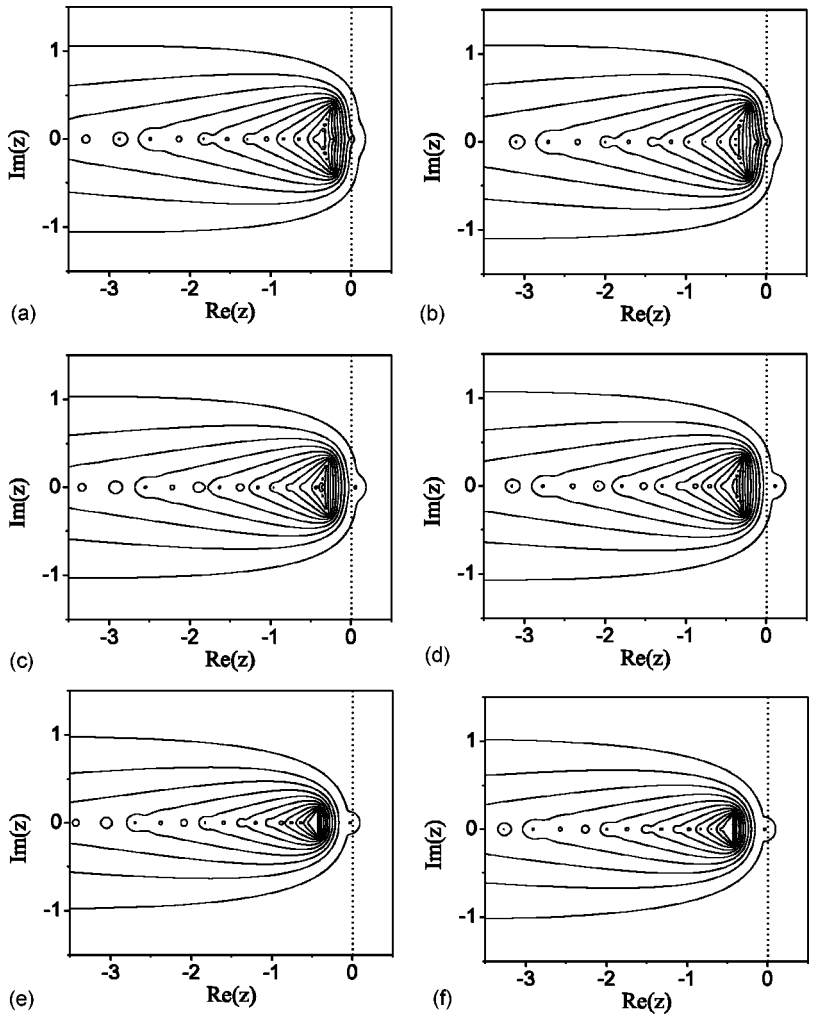

FIG. 9. Plots of the pseudospectra for three wave numbers. The abscissa is Re(z), and the ordinate is Im(z). Parameters values are (a) $\alpha=0.10$, $q=0.0$, (b) $\alpha=0.01$, $q=0.0$, (c) $\alpha=0.10$, $q=0.35$, (d) $\alpha=0.01$, $q=0.35$, (e) $\alpha=0.10$, $q=0.60$, and (f) $\alpha=0.01$, $q=0.60$. Here $\mathsf{C}_s=0.10$ for $\alpha=0.10$ and $\mathsf{C}_s=1.0$ for $\alpha=0.01$. Contours are plotted for $\epsilon=10^{-1},10^{-2},\ldots,10^{-11}$. The dotted vertical line separates the stable and unstable halves of the complex plane.

tional domains of various lengths. Direct computation of $\|\exp(t\mathbf{A})\|$ on the different domains confirms that the maximum amplification of disturbances is nearly identical for $t \leqslant 25$. For later times, the amplification of disturbances with small wave numbers increases as the length of the domain increases (because the pertinent optimal excitations encompass the entire spreading film), but this amplification is physically insignificant because modal growth dominates at these late times. Furthermore, the formulation of the problem in the "inner region" is valid only for distances of $\mathcal{O}(l)$ away from the contact line, so an infinite extension of the flat region of the film is not physical. In order to determine the height profile of the entire spreading film, the base-state profile must be matched to the profile in the "outer region." The variation of the viscosity and surface tension with temperature over this longer distance becomes appreciable and must be incorporated into the theoretical model.

The pseudospectra were also determined for a computational domain ending at $\xi=25$. Those results indicate an even smaller degree of non-normality, so the plots are not included here. The structure of the pseudospectra near $\mathrm{Re}(z)\approx 0$ is similar to that shown for the longer domain above and clearly indicates that the leading eigenvalue is physically determinant. In contrast to the plots computed on the domain $\xi\in[0,75]$, contours for $\epsilon<10^{-3.5}$ are not visible on the scale of the plot, which demonstrates that the (unphysical) longer domains cause an increase in the non-normality of the disturbance operator and can affect the accuracy of the computed eigenvalues around which contours with very small ϵ are visible.

VI. DISCUSSION

In agreement with results from analysis of a model employing a structured precursor film induced by purely attractive van der Waals forces [4] and from one employing a flat precursor film [3], there is little transient growth of perturbations, even for small values of the slip coefficient. In order for transient amplification to be significant [23], an initial perturbation with magnitude on the order of the microscopic length scale must be amplified to generate a macroscopic response on a time scale shorter than $1/\beta(q_{\max})$. As evident

from Fig. 5, only a small amount of transient amplification of any initial disturbance to the height profile occurs before the modal growth dominates. This limited transient amplification is therefore insufficient to introduce nonlinear effects that would invalidate the asymptotic results of the modal theory. The small transient spike at early times increases in magnitude as α decreases, but larger values of C_s, which result in larger modal growth rates, have almost no effect on the amount of initial transient amplification, although the maximum amount of nonmodal amplification, attained as $t \to \infty$, does increase.

Since the spectra for applied disturbances with wave numbers $q=0.0$ and $q=0.60$, for instance, are confined to the stable half-plane, the pseudospectra can be used to place a lower bound on the amount of growth that such a disturbance would experience. Applying Eq. (24) to the case with $\alpha=0.01$ and $C_s=1.0$ gives a lower bound of about 1.1 for $q=0.60$ and about 11 for $q=0.0$, while the actual values shown in Fig. 5 are 1.3 and 13, respectively. Note that since an applied disturbance with wave number $q=0.0$ does not vary in the transverse direction, such a disturbance is incapable of inducing instability.

The results of the transient analysis demonstrate that the ordering of the modes of different wave numbers according to amplification corresponds to the asymptotic results from the modal theory because the duration of nonmodal growth is short. These results also demonstrate a smooth, rapid transition to the asymptotic behavior predicted from the modal theory and therefore that the effects of the non-normality of the disturbance operators are slight.

The results of this investigation of a slip model agree well with results for models employing structured and unstructured precursor films to alleviate the contact line singularity [1,3,4]. Significant transient amplification is not found in any of the models for thermally driven films. The slip model has the smallest amount of transient amplification because all applied disturbances are truncated at the physical end of the domain at the contact line. More amplification occurs in the precursor film models because the applied disturbances can extend far into the precursor film and thus, as they are convected toward the apparent contact line, can repeatedly excite the most vulnerable area of the spreading film near the forward portion of the capillary ridge. This larger amount of transient amplification is still insufficient to invalidate the results of the modal theory, and plots of the pseudospectra for these models are similar to those for the slip model in that they do not exhibit a large degree of non-normality. Most significantly, the modal predictions of the slip model and flat precursor film model agree quantitatively for an appropriate choice of the contact slope and slip coefficient. The dispersion curves for the two models can be made to overlap almost exactly for the unstable wave numbers $q \lesssim 0.55$. This agreement between the slip and precursor film models was also found for coating flows driven by a body force [5]. Results from a model employing a structured precursor film governed by van der Waals forces [4] cannot be directly compared to the other two models because the inclusion of van der Waals forces is an additional stabilizing influence that slightly diminishes the growth rate of disturbances, but the qualitative results agree well. Finally, all three models predict an identical wavelength for the most unstable disturbance, and this value agrees quite well with published experimental results [1,17,24].

VII. CONCLUSION

The transient behavior of disturbances to and linear stability of thin, thermally driven films with slip at the liquid-solid interface have been investigated. The optimal disturbances for both asymptotically stable and unstable wave numbers initially have a peak of maximum amplitude at the contact line. Optimal disturbances that induce instability also broaden to encompass the entire capillary ridge. As $t \to \infty$ the evolved disturbances asymptote to the eigenfunction found from modal analysis, while the optimal initial disturbances asymptote to the corresponding eigenfunction of the adjoint of the linearized disturbance operator. Based on Figs. 5–8, this asymptotic limit is attained by a dimensionless time $t \approx 10-20$, which corresponds to the timescale reported in the literature for the onset of rivulet formation [17–19]. Although the slip model strongly influences the shapes of the optimal disturbances to the film, convergence of the disturbance growth rate to the asymptotic value found from the modal theory occurs rapidly for all disturbances. The limited transient amplification is insufficient to induce significant nonlinear effects, and this conclusion is reinforced by examination of plots of the pseudospectra of the linearized disturbance operator. For an appropriate choice of slip coefficient and contact slope, the base-state profiles and modal predictions of the flat precursor film model can be reproduced. The results from this study, along with those from two other investigations [3,4], indicate that the transient amplification of disturbances is relatively unimportant for thermally driven films and that, regardless of the contact line model, the non-normality of the linearized disturbance operator is insufficient to invalidate the modal results.

Note added in proof. After this work was completed, the authors became aware of an independent study of thermally driven films subject to boundary slip [25]. The different boundary conditions applied to the disturbance fields in Ref. [25] result in adjoint eigenfunctions rather different from those presented here.

ACKNOWLEDGMENTS

J.M.D. gratefully acknowledges financial support from the Air Force Office of Scientific Research and the Association of Princeton Graduate Alumni. S.M.T. kindly acknowledges the National Science Foundation (CTS and DMR divisions) and NASA.

[1] D. E. Kataoka and S. M. Troian, J. Colloid Interface Sci. **192**, 350 (1997).
[2] D. E. Kataoka and S. M. Troian, J. Colloid Interface Sci. **203**, 335 (1998).
[3] D. E. Kataoka, Ph.D. thesis, Princeton University, 1999.
[4] J. M. Davis and S. M. Troian, Phys. Rev. E **67**, 016308 (2003).
[5] M. A. Spaid and G. M. Homsy, Phys. Fluids **8**, 460 (1996).
[6] A. Oron, S. H. Davis, and S. G. Bankoff, Rev. Mod. Phys. **69**, 931 (1997).
[7] H. Greenspan, J. Fluid Mech. **84**, 125 (1978).
[8] P. J. Schmid, Phys. Plasmas **7**, 1788 (2000).
[9] D. H. Griffel, *Applied Functional Analysis* (Ellis Horwood Limited, Chichester, England, 1981).
[10] L. N. Trefethen, A. E. Trefethen, S. C. Reddy, and T. A. Driscoll, Science **261**, 578 (1993).
[11] P. J. Schmid and D. S. Henningson, *Stability and Transition in Shear Flows* (Springer-Verlag, New York, 2001).
[12] J. M. Davis, B. J. Fischer, and S. M. Troian, in *Interfacial Fluid Dynamics and Transport Properties*, Lecture Notes in Physics Series, edited by R. Narayananand D. Schwabe (Springer-Verlag, Berlin, 2003), p. 79.
[13] B. F. Farrell and P. J. Ioannou, J. Atmos. Sci. **53**, 2025 (1996).
[14] G. H. Golub and C. F. V. Loan, *Matrix Computations*, 2nd ed. (Johns Hopkins University Press, Baltimore, MD, 1990).
[15] L. N. Trefethen, SIAM Rev. **39**, 383 (1997).
[16] T. Kato, *Perturbation Theory for Linear Operators* (Springer-Verlag, New York, 1966).
[17] A. M. Cazabat, F. Heslot, S. M. Troian, and P. Carles, Nature (London) **346**, 824 (1990).
[18] P. Carles, S. M. Troian, A. M. Cazabat, and F. Heslot, J. Phys.: Condens. Matter **2**, SA477 (1990).
[19] J. B. Brzoska, F. Brochard-Wyart, and F. Rondelez, Europhys. Lett. **19**, 97 (1992).
[20] S. Kalliadasis, J. Fluid Mech. **413**, 355 (2000).
[21] T. G. Wright and L. N. Trefethen, SIAM J. Sci. Comput. (USA) **23**, 591 (2001).
[22] K. M. Butler and B. F. Farrell, Phys. Fluids A **4**, 1637 (1992).
[23] A. L. Bertozzi and M. P. Brenner, Phys. Fluids **9**, 530 (1997).
[24] P. Carles and A.-M. Cazabat, J. Colloid Interface Sci. **157**, 196 (1993).
[25] R. O. Grigoriev, Phys. Fluids **15**, 1363 (2003).